Analytical expression for mode-coupling coefficient between non-identical step-index cores and its application to multi-core fiber design within 125-μm cladding diameter

Yizhou Wang*, Takeshi Fujisawa, and Kunimasa Saitoh

Graduate School of Information Science and Technology, Hokkaido University, Sapporo 060-0814, Japan
*ywang@icp.ist.hokudai.ac.jp

ABSTRACT Analytical expression is derived for the mode-coupling coefficient between non-identical step-index (SI) cores, which enables a quick estimate of the crosstalk in the heterogeneous SI multi-core fibers (Hetero-SI-MCFs). The analytical results are in good agreement with the results obtained by numerical simulations by finite-element method (FEM). Using the derived analytical expression, the feasibility of Hetero-SI-MCF design within standard 125-μm cladding diameter is discussed. The designed MCFs have potential applications in space division multiplexing (SDM) systems.
key words: Standard cladding diameter, heterogeneous multicore fiber, step-index profile, space division multiplexing.

1. Introduction

As a promising implementation of space division multiplexing (SDM) [1], multi-core fibers (MCFs), in which multiple cores are packed in a single-fiber cladding, have been studied intensively. Inter-core crosstalk (XT), which leads to signal distortion is a severe issue in MCFs. To realize large core count while maintaining sufficiently low XT, many researches accepted cladding diameters larger than the standard 125-μm cladding diameter [2, 3]. However, because the mechanical reliability evidently degrades as the cladding diameter increases [3, 4], the standard cladding diameter is preferable for use in the tight bend situations. It is also known that MCFs with the standard cladding diameter enable the utilization of the existing optical cables, connector interfaces, and conventional optical components [5]. In addition, the already mature splicing and cabling technologies utilized for conventional single-core fibers can be applied to fabricate MCFs with the standard cladding diameter [4], effecting a reduction in the fabrication cost.

So far, two types of MCFs have mainly been proposed for use in transmission. One is the homogeneous MCF (Homo-MCF), in which all the cores are identical [2]; another one is the heterogeneous MCF (Hetero-MCF) which contains non-identical cores [3]. As compared with identical cores, non-identical cores can be more closely packed in a limited cladding diameter because the slight differences in their core radii and core refractive indices can make XT go down drastically. In addition, cores with a low refractive index trench-assisted (TA) profile are generally used for further suppressing XT [2-4, 6]. However, because the trenches are micrometer-sized structures and a large amount of fluorine dopant is required during the fabrication process [6], the fabrication becomes complex and expensive. Thus, using simple non-identical step-index (SI) cores is a potential means to reduce fabrication complexity and cost while achieving sufficiently low XT.

In general, to design MCFs, mode-coupling coefficients between the cores are required for estimating the average inter-core XT. Rigorous results can be obtained by numerical simulations. However, these are usually very time-consuming. Analytical expressions for the mode-coupling coefficients between non-identical cores have been reported in Refs. [7-9]. However, many of their results are derived using the coupled-mode theory or a complicated method, and their primary objective is to analyze the power transfer between non-identical cores. Moreover, the derived expressions have not been applied for designing MCFs. As another method, a simple two-core coordinate system has been successfully applied to derive the mode-coupling coefficients between identical SI cores [10], and a particularly simple expression has been derived. A similar coordinate system has been applied to derive the mode-coupling coefficients between non-identical TA cores [11]. However, because the modified Bessel functions of the first kind in the exact electric field expressions of the inner cladding and trench region are ignored for simplifying their derived expression,

a large error is seen in the mode-coupling coefficient when the trench region is relatively close to the core region [12]. To the best of our knowledge, the analytical expression for the mode-coupling coefficients between non-identical SI cores has not yet been formulated using the similar coordinate system, where the exact electric field expressions can be used and good accuracy can be expected.

Therefore, in this study, we first derive an analytical expression for the mode-coupling coefficient between non-identical SI cores using a simple two-core coordinate system. The integral in the original expression is simplified into a product of Bessel functions that can be easily calculated using mathematical tools. We then verify the validity of the derived expression for the cores effective in designing Hetero-SI-MCFs. The mode-coupling coefficients obtained by the derived analytical expression are in good agreement with the numerical simulations by finite-element method (FEM). This analytical expression is applied to design Hetero-SI-MCFs for various bandwidth operations, as described in Section 3-5, in which we estimate the XT values and analyze the XT variations for the fibers. A summary is presented in Section 6.

2. Mode coupling between non-identical cores

2.1 Derivation of analytical expression

The mode-coupling coefficient with the overlap integral of electromagnetic fields is generally written as follows [10]:

$$\kappa_{12} = \frac{\omega\varepsilon_0 \int_{-\infty}^{\infty}\int_{-\infty}^{\infty}\left(N^2 - {N_2}^2\right)\boldsymbol{E_1^*}\cdot\boldsymbol{E_2}dxdy}{\int_{-\infty}^{\infty}\int_{-\infty}^{\infty}\boldsymbol{u_z}\cdot(\boldsymbol{E_1^*}\times\boldsymbol{H_1}+\boldsymbol{E_1}\times\boldsymbol{H_1^*})dxdy} = \frac{\omega\varepsilon_0 \int_0^{2\pi}\int_0^{a}({n_1}^2 - {n_0}^2)\boldsymbol{E_1^*}\cdot\boldsymbol{E_2}rdrd\theta}{4\boldsymbol{P}}, \quad (1)$$

where κ_{12} represents the mode-coupling coefficient from core 2 to core 1. The subscripts 1 and 2 in Eq. (1) denote the parameters for core 1 and core 2, respectively. ω is the angular frequency of the electromagnetic fields and ε_0 is the permittivity of vacuum. $\boldsymbol{E}$ and $\boldsymbol{H}$ stand for the electric and magnetic fields, respectively, * denotes the complex conjugate, and $\boldsymbol{u}_z$ represents the unit vector of the z-axis. The denominator of the original function can be written as $4\boldsymbol{P}$, where $\boldsymbol{P}$ refers to the total power flow in core 1. As illustrated in Fig. 1, N^2(x, y) denotes the refractive index distribution in the entire coupled region, and ${N_2}^2$(x, y) represents the refractive index distribution of core 2, which consist of core 2 and the cladding region. Thus, the difference in refractive index inside core 1 is expressed as ${n_1}^2 - {n_0}^2$, where n_1 and n_0 represent the refractive indices of core 1 and the cladding, respectively.

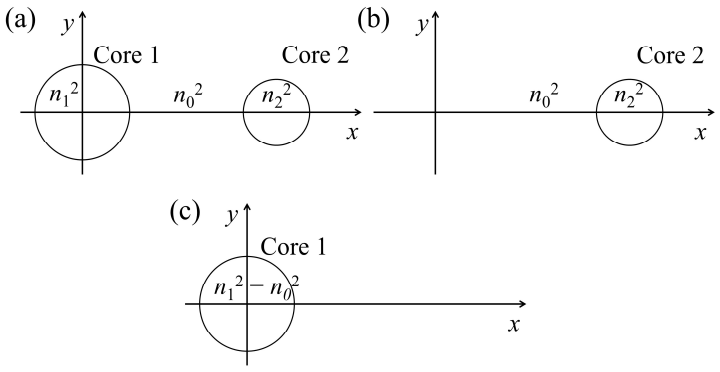

Fig. 1. Geometries for the calculation of κ_{12}. (a), (b), and (c) represent N^2(x, y), ${N_2}^2$(x, y), and N^2(x, y) − ${N_2}^2$(x, y), respectively.

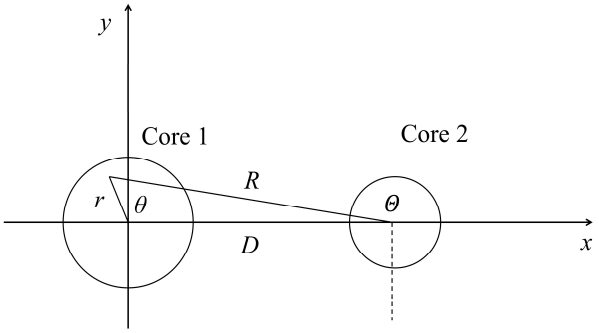

Fig. 2. Coordinate system for the calculation of κ_{12}. (R, Θ) is a coordinate system with its the origin at the center of core 2.

As illustrated in Fig. 2, to further simplify the numerator of Eq. (1), a coordinate system (R, Θ) whose origin is the center of core 2 is used, here D represents the core pitch. Hence, it is easy to consider the electric field in the core region of core 1 for $\boldsymbol{E}_1$ and the electric field in the cladding of core 2 for $\boldsymbol{E}_2$. The exact electric fields of the fundamental mode can be expressed by the following expressions [10].

Core region of core 1:

$$\begin{aligned} E_x &= C_1 J_0\left(\frac{U_1}{a_1} r\right) \cos\psi, \\ E_y &= -C_1 J_0\left(\frac{U_1}{a_1} r\right) \sin\psi, \\ E_z &= j\frac{U_1}{\beta_1 a_1} C_1 J_1\left(\frac{U_1}{a_1} r\right) \cos(\theta + \psi), \end{aligned} \tag{2}$$

Cladding region core 2:

$$\begin{aligned} E_x &= C_2 \frac{J_0(U_2)}{K_0(W_2)} K_0\left(\frac{W_2}{a_2} R\right) \cos\psi, \\ E_y &= -C_2 \frac{J_0(U_2)}{K_0(W_2)} K_0\left(\frac{W_2}{a_2} R\right) \sin\psi, \\ E_z &= j\frac{U_2}{\beta_2 a_2} C_2 \frac{J_1(U_2)}{K_1(W_2)} K_1\left(\frac{W_2}{a_2} R\right) \cos(\theta + \psi). \end{aligned} \tag{3}$$

As illustrated in Fig. 2, r denotes the distance from one point to the center of core 1 and R represents the distance from one point to the center of core 2. a_1 and a_2 denote the core radii of cores 1 and 2, respectively, U and W represent the normalized transverse wave numbers in the core and cladding region, respectively, and ψ denotes the phase. $J_n(z)$ represents the Bessel functions of the first kind, and $K_n(z)$ represents the modified Bessel functions of the second kind, where n = 0 or 1 represents the order of the Bessel functions. C_1 and C_2 are related to the power flow $\boldsymbol{P}$ and are expressed by Eq. (4.111) in [10]:

$$\begin{aligned} C_1 &= \frac{W_1}{a_1 V_1 J_1(U_1)} \sqrt{\frac{2\boldsymbol{P_1}}{\pi\varepsilon_0 n_1 c}}, \\ C_2 &= \frac{W_2}{a_2 V_2 J_1(U_2)} \sqrt{\frac{2\boldsymbol{P_2}}{\pi\varepsilon_0 n_2 c}}, \end{aligned} \tag{4}$$

where c is the velocity of light in vacuum, and V is the normalized frequency.

Therefore, $\boldsymbol{E}^*_1 \cdot \boldsymbol{E}_2$ in Eq. (1) is expressed as follows:

$$E_1^* \cdot E_2 = C_1 C_2 J_0\left(\frac{U_1}{a_1} r\right) \frac{J_0(U_2)}{K_0(W_2)} K_0\left(\frac{W_2}{a_2} R\right) + \frac{U_1 U_2}{\beta_1 \beta_2 a_1 a_2} C_1 C_2 J_1\left(\frac{U_1}{a_1} r\right) \frac{J_1(U_2)}{K_1(W_2)} K_1\left(\frac{W_2}{a_2} R\right) \cos(\theta + \psi) \cos(\Theta + \psi). \tag{5}$$

Because the second term on the right-hand side of Eq. (5) is sufficiently smaller than the first term, the integration term in the numerator becomes

$$S = \int_0^{2\pi} \int_0^a ({n_1}^2 - {n_0}^2) C_1 C_2 J_0\left(\frac{U_1}{a_1} r\right) \frac{J_0(U_2)}{K_0(W_2)} K_0\left(\frac{W_2}{a_2} R\right) r dr d\theta. \tag{6}$$

When $D >> r$, using the following approximation

$$R = \sqrt{D^2 + r^2 - 2Dr\cos\theta} \cong D - r\cos\theta, \tag{7}$$

and considering the case when the argument of the modified Bessel function $K_n(z)$ is large, it can be approximated as

$$K_n(z) \cong \sqrt{\frac{\pi}{2z}} exp(-z). \tag{8}$$

Therefore, using the following two integral formulas of Bessel functions:

$$I_0(z) = \frac{1}{\pi} \int_0^{\pi} \exp(z\cos\theta) d\theta, \tag{9}$$

$$\int_0^1 J_0(Uz) I_0(Wz) z dz = \frac{J_0(Uz) W I_1(Wz) + I_0(Uz) U J_1(Wz)}{U^2 + W^2}, \tag{10}$$

the integration term of the numerator is further written as:

$$S = 2\pi a_1^2({n_1}^2 - {n_0}^2)C_1C_2\frac{J_0(U_2)}{K_0(W_2)}\sqrt{\frac{\pi a_2}{2W_2D}}\,exp\left(-\frac{W_2}{a_2}D\right)\frac{J_0(U_1)W_2\frac{a_1}{a_2}I_1\left(U_2\frac{a_1}{a_2}\right)+I_0\left(W_2\frac{a_1}{a_2}\right)U_1J_1(U_1)}{{U_1}^2+\left(W_2\frac{a_1}{a_2}\right)^2}, \tag{11}$$

where $I_n(z)$ represents the modified Bessel functions of the first kind.

Here, we consider that core 2 is not so much different from core 1, so that $C_2 \backsimeq C_1$. The mode-coupling coefficient of core 2 to core 1 is finally given as follows:

$$\kappa_{12} = \frac{\omega\varepsilon_0 S}{4\boldsymbol{P}} = \frac{\sqrt{\Delta_1}}{a_2}\frac{W_1W_2}{V_2J_1(U_1)J_1(U_2)}\sqrt{\frac{\pi a_2}{W_2D}}\,exp\left(-\frac{W_2}{a_2}D\right)\frac{J_0(U_2)}{K_0(W_2)}\frac{J_0(U_1)W_2\frac{a_1}{a_2}I_1\left(U_2\frac{a_1}{a_2}\right)+I_0\left(W_2\frac{a_1}{a_2}\right)U_1J_1(U_1)}{{U_1}^2+\left(W_2\frac{a_1}{a_2}\right)^2}, \tag{12}$$

where Δ_1 is the relative core refractive index difference of core 1. By exchanging the subscripts 1 and 2 in Eq. (12), we obtain the mode-coupling coefficient from core 1 to core 2 (κ_{21}).

2.2 Estimation of XT between non-identical cores

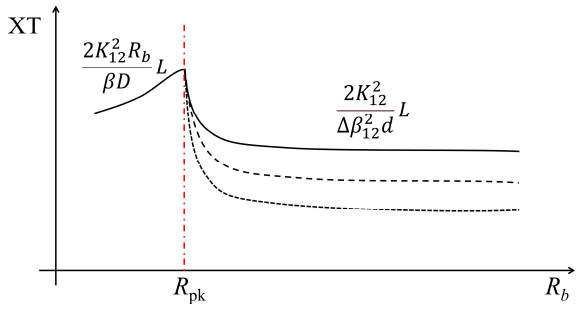

Fig. 3. Schematic of XT for Hetero-MCFs

As shown in Fig. 3, it is already known that the XT between non-identical cores drastically decreases to an ultra-low value at a critical bending radius (R_{pk}) and converges to this particular value no matter how the bending radius (R_{b}) increases. R_{pk} is given by the following equation [3].

$$R_{\mathrm{pk}} = \frac{n_{\mathrm{eff}}}{\Delta n_{\mathrm{eff}}}D, \tag{13}$$

where n_{eff} is the effective index of the mode, Δn_{eff} is the effective index difference between the non-identical cores, and D is the core pitch. As shown in Fig. 3, when $R_{\mathrm{b}} < R_{\mathrm{pk}}$, XT is given by [3]

$$\mathrm{XT} = \frac{2K_{12}^2R_b}{\beta D}L, \tag{14}$$

where K_{12} is the average value of the mode-coupling coefficients κ_{12} and κ_{21}, β is the propagation constant of the mode, and L is the transmission length. When $R_{\mathrm{b}} > R_{\mathrm{pk}}$, XT is given by [3]

$$\mathrm{XT} = \frac{2K_{12}^2}{\Delta\beta_{12}^2 d}L, \tag{15}$$

where $\Delta\beta_{12}$ is the difference in the equivalent propagation constant between the modes in cores 1 and 2. d is termed as the correlation length, and it strongly affects the XT value in the bending-insensitive region [3]. In this study, d is assumed to be larger than 1 m for the estimation of XT because both the experimentally measured data and numerical results proved that the value of d between non-identical cores is larger than 1 m [13, 14].

2.3 Application to MCF design

It is known that there is an effective core region (*ECR*) that is defined by the loss limits for designing MCFs [3, 5]. Outside this region, cores with very large core radii or very high relative core refractive indices yield the higher-mode, whereas very small

core radii or very low relative core refractive indices cause the loss of fundamental mode to be too large to be used. Therefore, in this section, we discuss the verification of the validity of the derived expression in the *ECR*. We compare the mode-coupling coefficients obtained by the derived analytical expression (K_{Ana}) with those obtained by FEM simulation (K_{FEM}) in the O- and C-band, respectively. The comparison indicates that the error in the XT obtained by the analytical expression and FEM is less than 2.0 dB/km.

The error in K_{12} is simply defined as the ratio of K_{Ana} to K_{FEM}, as expressed by the following equation:

$$e_K = \frac{K_{\mathrm{Ana}}}{K_{\mathrm{FEM}}}. \tag{16}$$

Therefore, the difference between the XT values obtained by the analytical expression ($\mathrm{XT_{Ana}}$) and those obtained by FEM simulation ($\mathrm{XT_{FEM}}$) can be given by

$$\mathrm{XT_{diff}} = \mathrm{XT_{Ana}} - \mathrm{XT_{FEM}} = 10\log_{10}(e_K^2). \tag{17}$$

For the O-band operation, a_1 is fixed as 4.1 μm with $\Delta_1 = 0.39\%$ because this is the core parameter with the maximized optical confinement that can be operated along the O-band [5], and it also indicates that core 2 should have $a_2 \leq 4.1$ μm with $\Delta_2 \leq 0.39\%$. Here we consider that a_2 ranges from 3.3 to 4.1 μm and Δ_2 ranges from 0.31% to 0.39%.

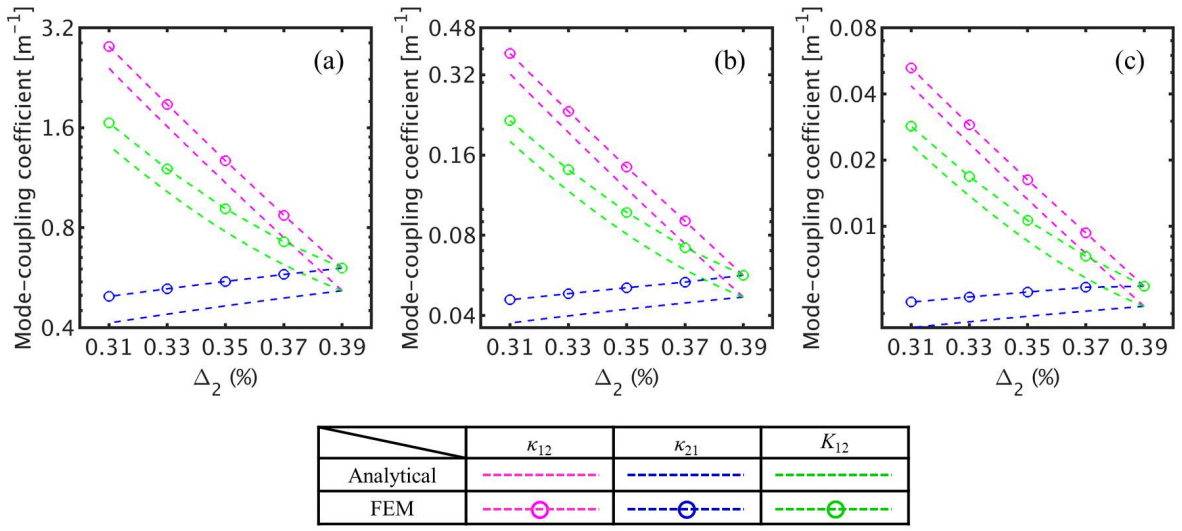

Fig. 4. Mode-coupling coefficients (κ_{12}, κ_{21}, and K_{12}) as functions of Δ_2 at $\lambda = 1310$ nm for D = (a) 25 μm, (b) 30 μm, and (c) 35 μm.

Figures 4 (a), (b), and (c) plot the mode-coupling coefficients (κ_{12}, κ_{21}, and K_{12}) as functions of Δ_2 at 1310 nm for D = 25, 30, and 35 μm, respectively, where $a_2 = a_1 = 4.1$ μm and Δ_2 ranges from 0.31% to 0.39%. The magenta, blue, and green dashed lines represent the analytical results of κ_{12}, κ_{21}, and K_{12}, respectively, and the magenta, blue, and green dashed lines with circles represent the FEM simulations of κ_{12}, κ_{21}, and K_{12}, respectively. We can see that the analytical results have the same trend as the FEM simulations. Due to the mode confinement becomes better, κ_{12} decreases as Δ_2 increases, whereas κ_{21} increases a little as Δ_2 increases because there is a small increase in the difference between the refractive indices. When $\Delta_2 = 0.39\%$, core 2 is identical to core 1, leading to $\kappa_{12} = \kappa_{21} = K_{12}$, which are represented by the rightmost green circles. Here, because the last term of Eq. (5) is ignored during the derivation, all the analytical results are smaller than those obtained by FEM simulations. The minimum value of e_K is 79% in Fig. 4, which is relatively high for a mode-coupling coeffecient. However, if we substitute this value into Eq. (17), the $\mathrm{XT_{diff}}$ can be expected to be less than 2.0 dB/km.

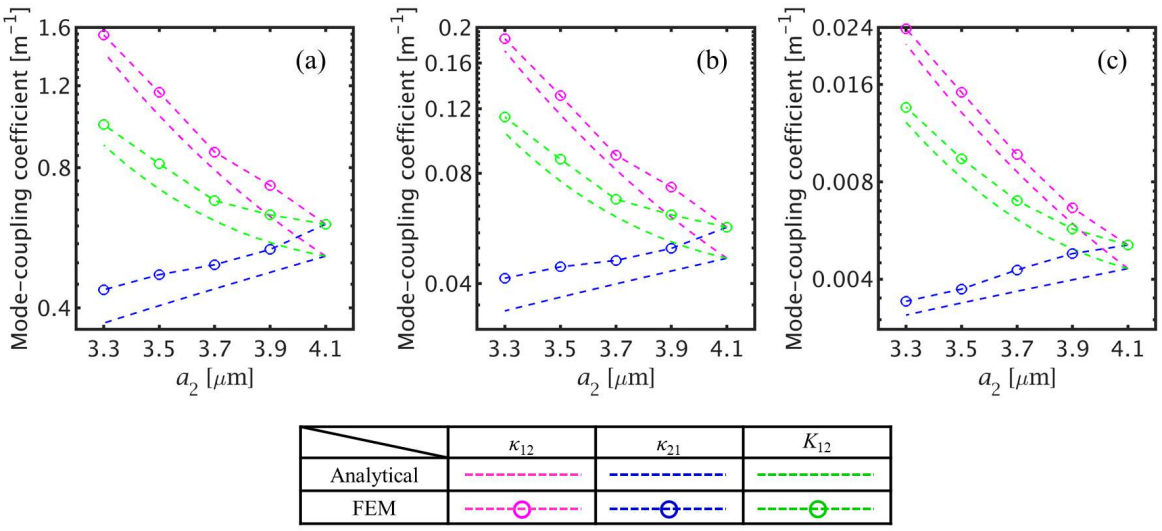

Fig. 5. Mode-coupling coefficients (κ_{12}, κ_{21}, and K_{12}) as functions of a_2 at λ = 1310 nm for D = (a) 25 μm, (b) 30 μm, and (c) 35 μm.

Figures 5 (a), (b), and (c) plot the mode-coupling coefficients as functions of a_2 at 1310 nm for D = 25, 30, and 35 μm, respectively, where $\Delta_2 = \Delta_1 = 0.39\%$ and a_2 ranges from 3.3 to 4.1 μm. We can also see high accuracy in the analytical results and FEM simulations, and κ_{12}, κ_{21}, and K_{12} show the same trend as that depicted in Fig. 4. The difference between K_{Ana} and K_{FEM} increases as the core radius increases because Eq. (7) is used in the derivation of the analytical expression, in the case of the fixed core pitch, it is more accurate when the core radius is small. Here, the minimum value of e_K is 82%, leading the value of XT_{diff} to be less than 1.7 dB/km.

Owing to the strict loss requirements, it is easy to see that the largest core radius that can be used for C-band operation is approximately 4.9 μm with the highest relative core refractive index of approximately 0.42% from the Fig. 10 in Ref. [3]. Accordingly, we fix a_1 as 4.9 μm with $\Delta_1 = 0.42\%$ and change a_2 from 4.1 to 4.9 μm and Δ_2 from 0.34% to 0.42% to verify the validity.

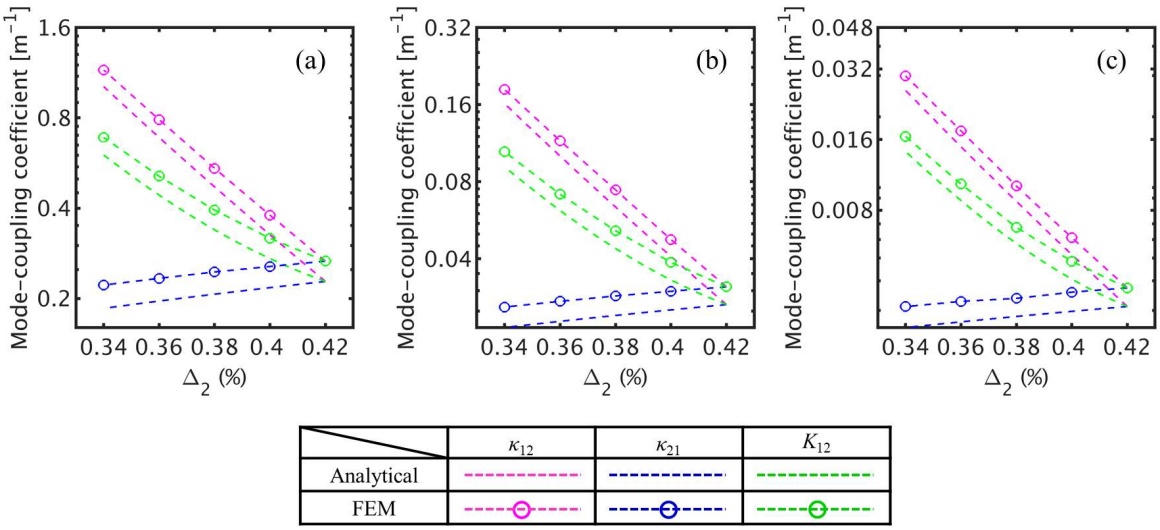

Fig. 6. Mode-coupling coefficients (κ_{12}, κ_{21}, and K_{12}) as functions of Δ_2 at λ = 1550 nm for D = (a) 30 μm, (b) 35 μm, and (c) 40 μm.

Figures 6 (a), (b), and (c) plot the mode-coupling coefficients as functions of Δ_2 at 1550 nm for D = 30, 35, and 40 μm, respectively, where $a_2 = a_1 = 4.9$ μm and Δ_2 ranges from 0.34% to 0.42%. We can also see that the analytical results indicate the same trend as the FEM simulations. Here, the minimum value of e_K is 84%, leading the value of XT_{diff} to be less than 1.5 dB/km.

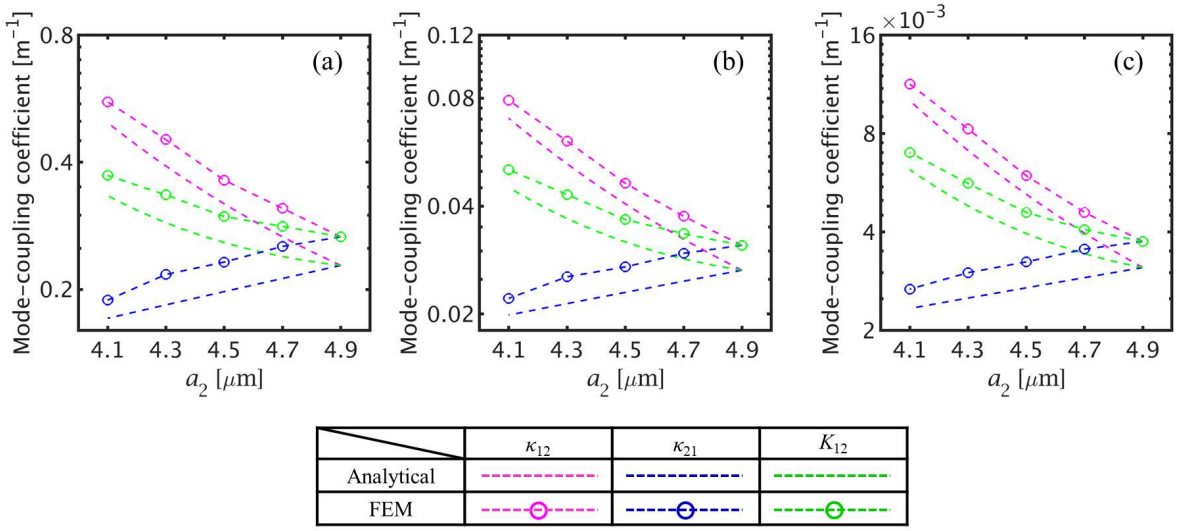

Fig. 7. Mode-coupling coefficients (κ_{12}, κ_{21}, and K_{12}) as functions of a_2 at λ = 1550 nm for D = (a) 30 μm, (b) 35 μm, and (c) 40 μm.

Figures 7 (a), (b) and (c) plot the mode-coupling coefficients as functions of a_2 at 1550 nm for D = 30, 35, and 40 μm, respectively, where $\Delta_2 = \Delta_1 = 0.42\%$ and a_2 ranges from 4.1 to 4.9 μm. We can also see that the difference between K_{Ana} and K_{FEM} increases as the core radius increases, which can be attributed to the fact that Eq. (7) is more accurate for a smaller core radius when the core pitch is fixed. Here, the minimum value of e_K is 84%, leading the value of $\mathrm{XT}_{\mathrm{diff}}$ to be less than 1.5 dB/km.

Therefore, the XT values obtained by the analytical expression are considered to be 2.0 dB/km lower than those obtained by FEM simulations. In the following sections, this expression is applied to quickly estimate the XT values of MCFs.

3. Fiber design for O-band

References [4] and [6] have reported eight-core fibers with 125-μm cladding diameter for O-band use. However, the sufficiently low XT is realized by TA profile. Here, we attempt to use the simple SI profile for easy fabrication. Furthermore, due to the overlap of TA structures, the number of cores reported in Refs. [4] and [6] reached the upper limit of 8. The simple SI cores facilitate a further increase in the number of cores within the limited diameter.

3.1 Selection of core parameters

Figures 8 (a) and (b) show the general method of core selections. Cores with different core radii (a) and relative refractive indices (Δ) have different effective areas (A_{eff}). For realizing the homogeneity of the transmission characteristics and low splice losses [3], cores with similar values of A_{eff} must be selected. In this study, we select cores with $A_{\mathrm{eff}} = 55$ μm^2 at λ = 1310 nm, which is comparable to the effective area of the cores reported in Refs. [4, 6] and is represented by the black dashed line.

As the bending loss (BL) of the cores is strongly affected by the outer cladding thickness (T_{C}) [2], we start with a T_{C} of 25 μm and increase it in steps of 1 μm to select the cores for fiber design. To guarantee single-mode operation, the colored dashed lines represent the cutoff limits of LP_{11} mode for different values of T_{C}, which are plotted by assuming the BL of LP_{11} mode to be larger than 1 dB/m at λ = 1260 nm and R_{b} = 140 mm, whereas the colored solid lines represent the excessive loss (EL) limits of LP_{01} mode for different values of T_{C}, which are plotted by assuming the BL of LP_{01} mode to be less than 0.01 dB/km at λ = 1310 nm and R_{b} = 140 mm [4, 6]. The black dotted lines represent the constant n_{eff}s at λ = 1310 nm. Based on these curves, it can be seen that only cores in the region surrounded by the dashed and solid lines of the same color and on the $A_{\mathrm{eff}} = 55$ μm^2 line are effective for fiber design. This region is termed as effective core region (ECR).

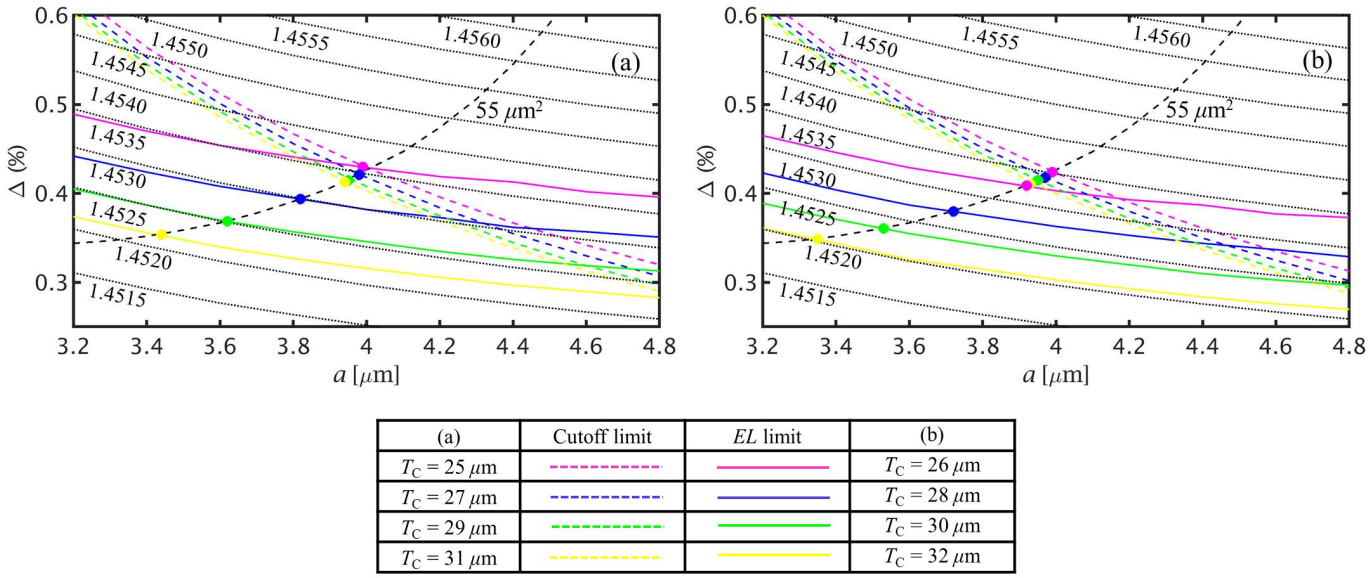

Fig. 8. Relationship between the core parameters and effective indices for the O-band: (a) T_C = 25, 27, 29, and 31 μm; (b) T_C = 26, 28, 30, and 32 μm.

As shown in Fig. 8 (a), when T_C = 25 μm, the *EL* and cutoff limits intersect at the magenta dot at which A_{eff} = 54.6 μm^2. Although the value of A_{eff} is slightly less than the target of 55 μm^2, we use this core to design homogeneous step-index MCFs (Homo-SI-MCFs). Furthermore, it is found that the *EL* and cutoff limits are shifted to the lower core refractive region as T_C increases, and the *EL* limits descend more rapidly than the cutoff limits. This is because the loss of LP_{01} mode is more sensitive to T_C than that of LP_{11} mode, which leads to the enlargement of the *ECR*, facilitating the selection of non-identical cores to design Hetero-SI-MCFs.

Further, based on Eq. (13), a larger value of Δn_{eff} is able to achieve a smaller value of R_{pk}, which indicates that the XT will decrease to a low value more rapidly. Therefore, we use one core at the upper limit of *ECR* and another one core at the lower limit of *ECR* to design Hetero-SI-MCFs. For example, the two blue dots marked in Fig. 8 (a) are used for designing Hetero-SI-MCF with T_C = 27 μm, and other dots of the same color marked in Fig. 8 (a) and (b) denote the core combinations for designing Hetero-SI-MCF with different values of T_C. Moreover, it is clear that all the cores are within the range verified in Section 2. 3, facilitating the estimation of the XT values by the derived expression directly.

3.2 Achievable XT

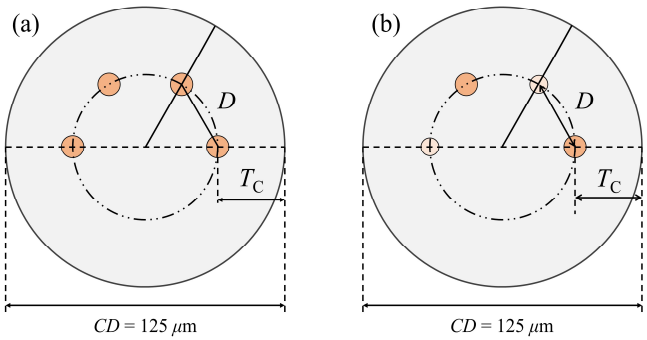

Fig. 9. Cross sections of the designed MCFs: (a) Homo-SI-MCFs with identical cores and (b) Hetero-SI-MCFs with non-identical cores.

Owing to restricted loss requirements, the cores have to be allocated as one-ring layout in the cladding as shown in Fig. 9. When the number of cores (N_c) is determined, the core pitch can be calculated using the following equation.

$$D = 2(CD/2 - T_C)\sin(\pi/N_c), \tag{18}$$

where *CD* represents the cladding diameter and is fixed as 125 μm. Therefore, using Eq. (14) and Eq. (15), the XT between two adjacent cores of the designed MCFs can easily be estimated.

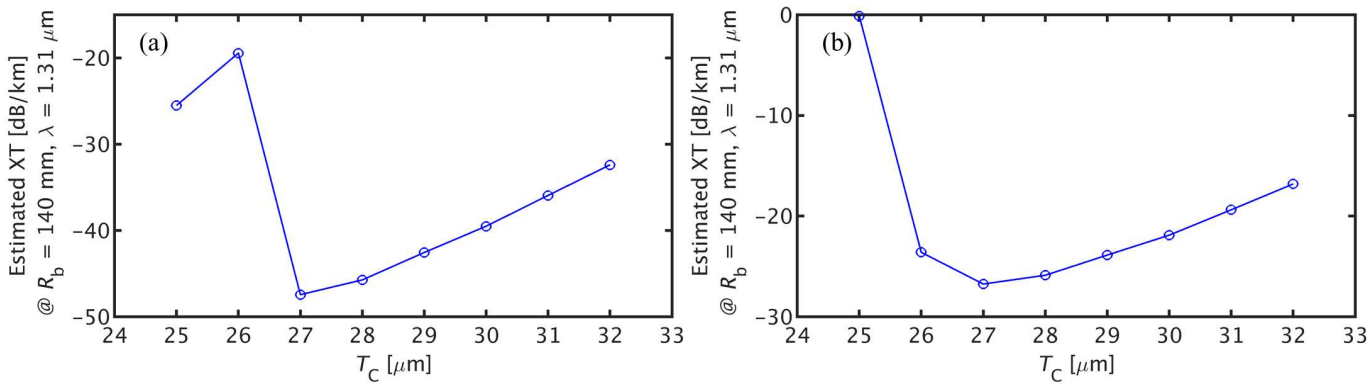

Fig. 10. Estimated nearest XT as functions of T_C for the O-band: (a) N_c = 8; (b) N_c = 10.

Figures 10 (a) and (b) plot the estimated nearest XT by the derived expression as functions of T_C for N_c = 8 and 10, respectively, where XT is estimated at λ = 1.31 μm and R_b = 140 mm, and d is assumed to be 1 m. When T_C = 25 μm, the XT of the Homo-SI-MCFs designed using the core represented by the magenta dot marked in Fig. 8 (a) is plotted. When T_C > 25 μm, the XT of the Hetero-SI-MCFs designed using the core combinations represented by the same color depicted in Fig. 8 (a) and (b) is plotted.

For N_c = 8, XT is relatively high when T_C < 27 μm. This is because the R_{pk} of Hetero-SI-MCFs is larger than 140 mm. When T_C reaches 27 μm, the R_{pk} of Hetero-SI-MCFs is smaller than 140 mm, leading to a drastic decrease in the XT. Thereafter, the XT increases as T_C increases because K_{12} increases rapidly as T_C increases. The best value of the nearest XT is −47.3 dB/km at T_C = 27 μm, because multiple cores are incorporated in one single-fiber cladding, we consider that the total XT for each core is equivalently caused by two neighboring cores, leading to a 3-dB/km increase in the total XT. Since it is already known that for a 1-dB XT penalty, the average XT levels of −16 dB are allowed for QPSK format signals [15], this eight-core fiber can be expected to support at least hundreds of kilometers of transmission.

For N_c = 10, when T_C < 27 μm, XT is relatively high because the R_{pk} of Hetero-SI-MCF is larger than 140 mm. When T_C reaches 27 μm, XT decreases into a low value owing to the small R_{pk} of Hetero-SI-MCFs. The best value of the nearest XT is −26.6 dB/km at T_C = 27 μm. Considering a 2-dB/km increase in the XT owing to the error in the analytical expression and a 3-dB/km increase in it because of the two adjacent cores, the total XT value is −21.6 dB/km, which can be expected to support the transmission of QPSK format signals over 3 km [15]. This is the first description of a ten-core fiber with 125-μm cladding diameter for O-band operation.

4. Fiber design for C-band

Reference [5] has reported that 125-μm cladding diameter supports four identical SI cores with XT of −28 dB/km at λ = 1550 nm. In this study, non-identical SI cores are adopted to increase the number of cores and suppress the XT in the C-band.

4.1 Selection of core parameters

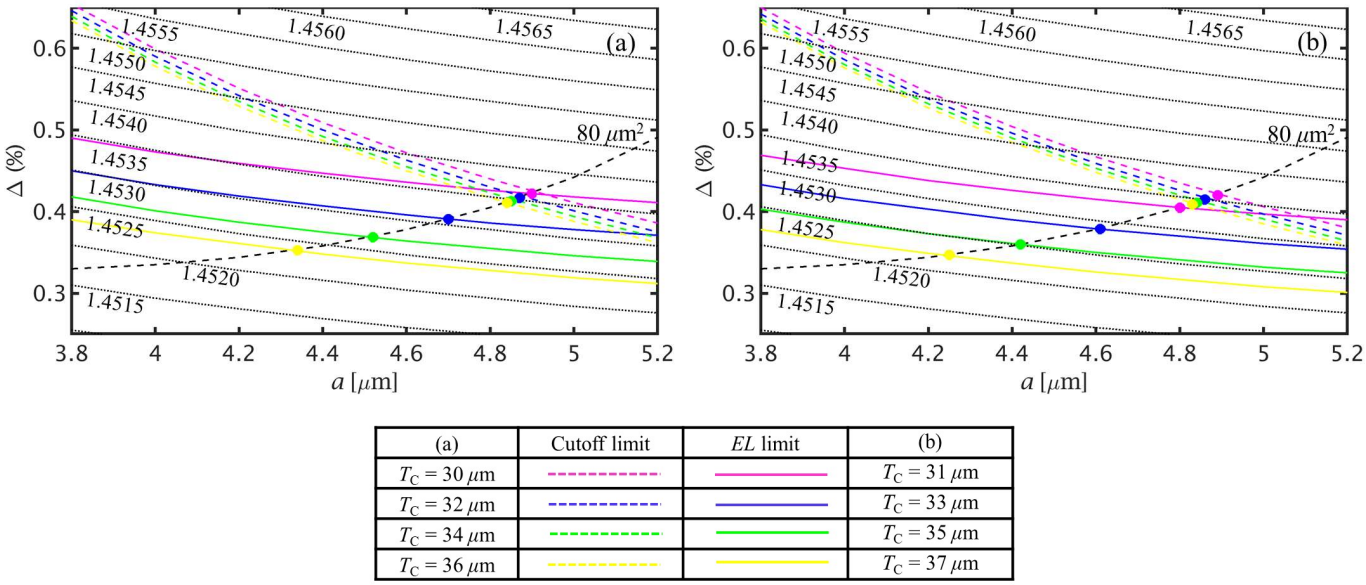

Fig. 11. Relationship between the core parameters and effective indices for the C-band: (a) T_C = 30, 32, 34, and 36 μm; (b) T_C = 31, 33, 35, and 37 μm.

For C-band use, T_C is initialized at 30 μm and increased to 37 μm in steps of 1 μm. The cutoff limits of LP_{11} mode are assumed to be larger than 1 dB/m at λ = 1530 nm and R_b = 140 mm, whereas the *EL* limits of LP_{01} mode are assumed be less than 0.01 dB/km at λ = 1565 nm and R_b = 140 mm [5]. The colored dashed and solid lines represent the cutoff and *EL* limits for the different values of T_C, respectively. The black dotted lines represent the constant n_{eff}s at λ = 1550 nm, and the black dashed line represents A_{eff} = 80 μm^2 at λ = 1550 nm, which is the general recommendation for single-core single-mode fibers.

When T_C = 30 μm, the *EL* limit, cutoff limit, and A_{eff} = 80 μm^2 line intersect at the magenta dot marked in Fig. 11 (a), indicating that this core can be used to design Homo-SI-MCFs. We can also find the enlargement of *ECR* as T_C increases, and the dots of the same color marked in Fig. 11 (a) and (b) are used for Hetero-SI-MCFs design. It is also clear that all the cores are within the range verified in Section 2. 3, facilitating the estimation of the XT values by the derived expression directly.

4.2 Achievable XT

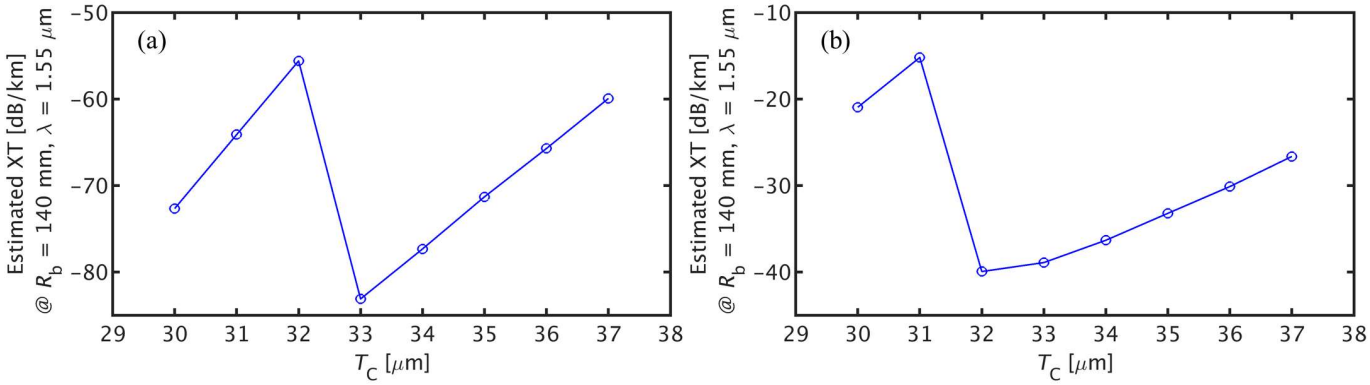

Fig. 12. Estimated nearest XT as functions of T_C for the C-band: (a) N_c = 4; (b) N_c = 6.

Figures 12 (a) and (b) plot the estimated nearest XT by the derived expression as functions of T_C for N_c = 4 and 6, respectively, in which the XT is estimated at λ = 1.55 μm and R_b = 140 mm, and d is assumed to be 1 m. When T_C = 30 μm, the XT of the Homo-SI-MCFs designed using the core represented by the magenta dot marked in Fig. 11 (a) is plotted, when T_C > 30 μm, the XT of the Hetero-SI-MCFs designed using the core combinations represented by the same color depicted in Fig. 11 (a) and (b) is plotted.

For N_c = 4, when T_C < 33 μm, the XT is relatively high because the R_{pk} of Hetero-SI-MCFs is larger than 140 mm. When T_C reaches 33 μm, XT drastically decreases into a low value because the R_{pk} of Hetero-SI-MCFs is smaller than 140 mm. The best value of the nearest XT is −83.0 dB/km at T_C = 33 μm, yielding a total XT of −78.0 dB/km, which can be expected to have negligible

impact on the transmission performance [5]. In comparison with the four-core fiber reported in Ref. [5], the XT value is significantly improved.

For $N_c = 6$, when $T_C < 32$ μm, the XT is relatively high because the R_{pk} of Hetero-SI-MCFs is larger than 140 mm. When T_C reaches 32 μm, the XT drastically decreases into a low value because the R_{pk} of Hetero-SI-MCFs is smaller than 140 mm. The best value of the nearest XT is −39.7 dB/km at $T_C = 32$ μm, yielding a total XT of −34.7 dB/km, which is expected to support the transmission of QPSK format signals with a XT penalty of 1 dB at approximately 70 km [15]. Thus, for the C-band, by using the non-identical SI cores, the number of cores is increased by 2, and the XT value exceeds that of the Homo-SI-MCFs reported in Ref. [5].

5. Fiber design for C+L-band

The four-core Homo-SI-MCF reported in Ref. [5] has a relatively high XT of −20 dB/km at λ = 1625 nm. In this study, we also attempt to adopt non-identical SI cores to increase the number of cores and suppress the XT in the C+L-band.

5.1 Selection of core parameters

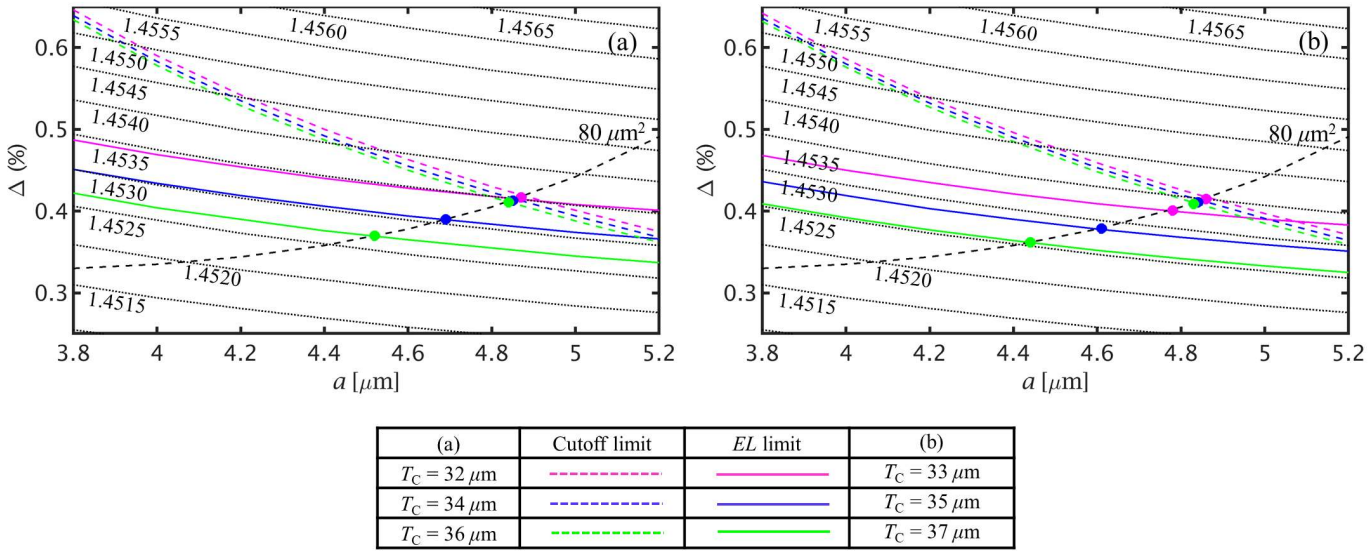

(a)	Cutoff limit	*EL* limit	(b)
$T_C = 32$ μm			$T_C = 33$ μm
$T_C = 34$ μm			$T_C = 35$ μm
$T_C = 36$ μm			$T_C = 37$ μm

Fig. 13. Relationship between the core parameters and effective indices for the C+L-band: (a) $T_C = 32$, 34, and 36 μm; (b) $T_C = 33$, 35, and 37 μm.

For C+L-band use, the cutoff limits are the same as those for the C-band use and are represented by the colored dashed lines in Fig. 13 (a) and (b), whereas the *EL* limits of LP_{01} mode are shifted to λ = 1625 nm and are represented by the colored solid lines. The black dotted and solid lines represent the same parameters as those for the C-band.

In this case, T_C is initialized at 32 μm and increased to 37 μm in steps of 1 μm. The *EL* limit, cutoff limit, and $A_{eff} = 80$ μm^2 line intersect at the magenta dot marked in Fig. 13 (a) when $T_C = 32$ μm, indicating that this core can be used to design Homo-SI-MCFs. It is also clear that the *ECR* is enlarged as T_C increases, and the core combinations represented by the dots of the same color depicted in Fig. 13 (a) and (b) are used for designing the Hetero-SI-MCFs. We can also find that the core parameters for the C+L band are almost the same as those for the C-band. As the wavelength for XT estimation does not change too much, the derived expression is directly used to estimate the XT values.

5.2 Achievable XT

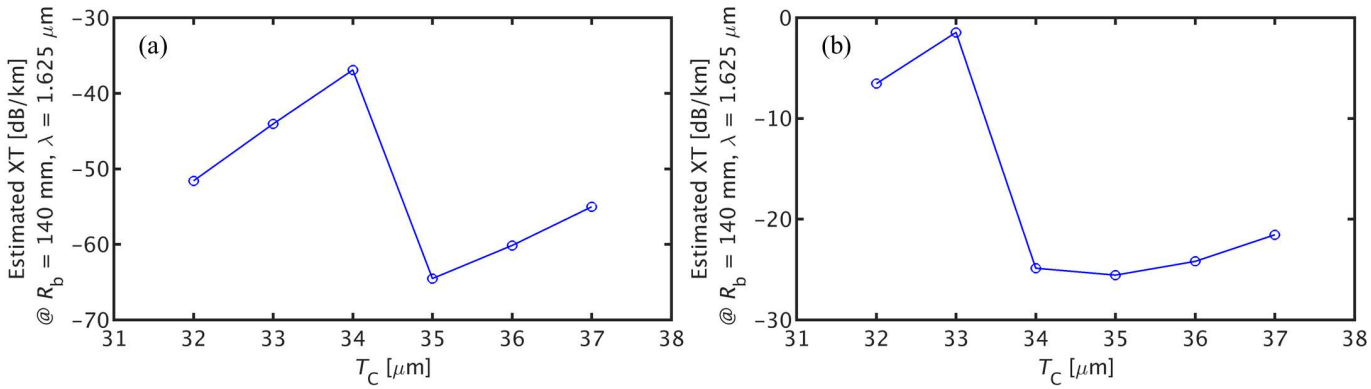

Fig. 14. Estimated nearest XT as functions of T_C for C+L-band use: (a) $N_c = 4$; (b) $N_c = 6$.

Figures 14 (a) and (b) plot the estimated nearest XT by the derived expression as functions of T_C for $N_c = 4$ and 6, respectively, where XT is estimated at $\lambda = 1.625$ μm and $R_b = 140$ mm, and d is assumed as 1 m. When $T_C = 32$ μm, the XT of the Homo-SI-MCFs designed using the core represented by the magenta dot marked in Fig. 13 (a) is plotted. When $T_C > 32$ μm, the XT of the Hetero-SI-MCFs designed using the core combinations represented by the same color depicted in Fig. 13 (a) and (b) is plotted.

For $N_c = 4$, when $T_C < 35$ μm, XT is relatively high because the R_{pk} of Hetero-SI-MCFs is larger than 140 mm. When T_C reaches 35 μm, XT drastically decreases into a low value because the R_{pk} of Hetero-SI-MCFs is smaller than 140 mm. The best value of the nearest XT is −64.5 dB/km at $T_C = 35$ μm, yielding a total XT of −59.5 dB/km, which can be also expected to have negligible impact on the transmission performance [5].

For $N_c = 6$, when $T_C < 34$ μm, XT is relatively high because the R_{pk} of Hetero-SI-MCF is larger than 140 mm. When T_C reaches 34 μm, XT drastically decreases into a low value because the R_{pk} of Hetero-SI-MCFs is smaller than 140 mm. The best value of the nearest XT is −25.5 dB/km at $T_C = 35$ μm, yielding a total XT of −20.5 dB/km, which supports the transmission of QPSK format signals with a XT penalty of 1 dB at approximately 3 km [15]. Similar to the fiber designed for the C-band, the non-identical SI cores enable us to add two more cores and improve the XT value in the C+L-band.

6. Conclusion

An analytical expression for the mode-coupling coefficient between non-identical SI cores is derived, which enables us to quickly estimate the XT values in Hetero-SI-MCFs without the need of numerical simulations. The derived analytical expression has a good accuracy as compared with the most rigorous numerical simulations by FEM. Therefore, it is a useful tool for the design of Hetero-SI-MCFs.

Using the derived analytical expressions, it has been shown that the simple SI profile enables us to allocate 10 and 6 non-identical cores in the 125-μm cladding diameter for the O- and C+L-bands, respectively, and the achieved XT values support several to hundreds of kilometers transmission of QPSK format signals with a XT penalty of 1 dB or less.

References

[1] T. Morioka, “New generation optical infrastructure technologies: ‘EXAT Initiative’ Towards 2020 and Beyond,” *Proc. Opt. Electron. Commun. Conf. (OECC)*, Paper FT4, July 2009.

[2] K. Takenaga, Y. Arakawa, Y. Sasaki, S. Tanigawa, S. Matsuo, K. Saitoh, and M. Koshiba, “A large effective area multi-core fiber with an optimized cladding thickness,” *Opt. Exp.*, vol. 19, no. 26, pp. B543–B550, Dec. 2011.

[3] S. Matsuo, K. Takenaga, Y. Sasaki, Y. Amma, S. Saito, K. Saitoh, T. Matsui, K. Nakajima, T. Mizuno, H. Takara, Y. Miyamoto, and T. Morioka, “High-spatial-multiplicity multicore fibers for future dense space-division-multiplexing systems,” *J. Lightw. Technol.*, vol. 34, no. 6, pp. 1464–1475, Mar. 2016.

[4] T. Hayashi, T. Nakanishi, K. Hirashima, O. Shimakawa, F. Sato, K. Koyama, A. Furuya, Y. Murakami, and T. Sasaki, “125-μm-cladding eight-core multi-core fiber realizing ultra-high-density cable suitable for O-band short-reach optical interconnects,” *J. Lightw. Technol.*, vol. 34, no.1, pp. 85–92, Jan. 2016.

[5] T. Matsui, Y. Sagae, T. Sakamoto, and K. Nakajima, “Design and applicability of multi-core fibers with standard cladding diameter,” *J. Lightw. Technol.*, vol. 38, no. 21, pp. 6065–6070, Nov. 2020.

[6] Y. Sasaki, M. Ozeki, K. Takenaga, and K. Aikawa, “Asymmetrically arranged 8-core fibers with center core suitable for side-view alignment in datacenter networks,” *Proc. Opt. Fiber Commun. Conf. (OFC)*, Paper T4J.1, Feb. 2020.

[7] P. D. Mcintyre, and A. W. Snyder, “Power transfer between optical fibers,” *J. Opt. Soc. Am.*, vol. 63, no. 12, pp. 1518–1527, 1973.

[8] A. W. Snyder, and A. Ankiewicz, “Optical fiber couplers-optimum solution for unequal cores,” *J. Lightw. Technol.*, vol. 6, no. 3, pp. 463–474, 1988.

[9] H. S. Huang, and H. -C. Chang, “Analysis of optical fiber directional coupling based on the HE_{11} modes-part II: the nonidentical-core case,” *J. Lightw. Technol.*, vol. 8, no. 6, pp. 832–837, Jun. 1990.

[10] K. Okamoto, *Fundamentals of Optical Waveguides*, 2nd ed. (Academic Press. 2006).

[11] J. Tu, K. Saitoh, M. Koshiba, K. Takenaga, and S. Matsuo, "Design and analysis of large-effective-area heterogeneous trench-assisted multi-core fiber," *Opt. Exp.*, vol. 20, no. 14, pp. 15157–15170, July. 2012.
[12] J. Tu, K. Saitoh, M. Koshiba, K. Takenaga, and S. Matsuo, "Optimized design method for bend-insensitive heterogeneous trench-assisted multi-core fiber with ultra-low crosstalk and high core density," *J. Lightw. Technol.*, vol. 31, no. 15, pp. 2590–2598, Aug. 2013.
[13] Y. Amma, Y. Sasaki, K. Takenaga, S. Matsuo, J. Tu, K. Saitoh, M. Koshiba, T. Morioka, and Y. Miyamoto, "High-density multicore fiber with heterogeneous core arrangement," *Proc. Opt. Fiber Commun. Conf. (OFC)*, Paper Th4C.4, Mar. 2015.
[14] T. Fujisawa, Y. Amma, Y. Sasaki, S. Matsuo, K. Aikawa, K. Saitoh, and M. Koshiba, "Crosstalk analysis of heterogeneous multicore fibers using coupled-mode theory," *IEEE Photon. J.*, vol. 9, no. 5, pp. 7204108, Oct. 2017.
[15] P. J. Winzer, A. H. Gnauck, A. Konczykowska, F. Jorge, and J. Y. Dupuy, "Penalties from in-band crosstalk for advanced optical modulation formats," *Proc. Eur. Conf. Exhib. Opt. Commun. (ECOC)*, Paper Tu.5.B.7, Sep. 2011.